Advanced Energy Materials

ADVANCED ENERGY MATERIALS
www.advenergymat.de

RESEARCH ARTICLE OPEN ACCESS

Enhanced Fast-Charging Performance of High-Mass-Loading Mn-Rich $Li[Mn_{1-x}Fe_x]PO_4$ Cathodes via LiF-Less Cathode–Electrolyte Interphase

Bonyoung Ku[1,2] | Lahyeon Jang[1,2] | Hyunji Kweon[1,2] | Jinho Ahn[1,2] | Sunha Hwang[1,2] | Jihoe Lee[1,2] | Myungeun Choi[1,2] | Sunyoung Yoo[3] | Kwangho Yoo[3] | Kyu-Young Park[4,5] | Jongsoon Kim[1,2]

[1]Department of Energy Science, Sungkyunkwan University, Suwon, Republic of Korea | [2]SKKU Institute of Energy Science and Technology, Sungkyunkwan University, Suwon, Republic of Korea | [3]Advanced Automotive Battery Development Center, LG Energy Solution, Daejeon, Republic of Korea | [4]Department of Materials Science and Engineering, Pohang University of Science and Technology, Pohang, Republic of Korea | [5]Department of Battery Engineering, Graduate Institute of Ferrous & Eco Materials Technology (GIFT), Pohang University of Science and Technology University, Pohang, Republic of Korea

Correspondence: Kyu-Young Park (kypark0922@postech.ac.kr) | Jongsoon Kim (jongsoonkim@skku.edu)

Received: 31 October 2025 | **Revised:** 1 January 2026 | **Accepted:** 16 January 2026

Keywords: cathode | fast-charging | $Li[Mn_{1-x}Fe_x]PO_4$ | Li-ion batteries | olivine

ABSTRACT

Mn-rich $Li[Mn_{1-x}Fe_x]PO_4$ (LMFP) cathodes are promising candidates for next-generation lithium-ion batteries due to their structural stability and cost-effectiveness. However, under industrially relevant high-mass-loading conditions, they still suffer from severe performance degradation, particularly during fast charging. In this study, we systematically demonstrate that charge-transfer resistance, rather than bulk Li^+ diffusivity, governs the kinetic limitations of LMFP electrodes with an areal capacity of ~3.5 mAh cm^{-2} (~23 mg cm^{-2} mass loading). Surface analyses reveal that the buildup of electronically and ionically insulating LiF at the cathode–electrolyte interphase (CEI) is the primary cause of sluggish charge transfer, highlighting a previously overlooked detrimental role of LiF. Guided by this insight, we implement an interfacial engineering strategy that suppresses LiF formation at the CEI. Remarkably, the resulting high-mass-loading LMFP cathodes deliver a 1.6-fold increase in capacity at 5C and retain ~87% of their initial capacity after 100 cycles at 2C. Moreover, *operando* structural analysis reveals that electrodes with LiF-suppressed CEI maintain a robust single-phase transition during fast cycling, directly linking interfacial LiF suppression to significantly enhanced charge-transfer kinetics. This work highlights the critical importance of CEI engineering in enabling fast-charging Mn-rich olivine cathodes under practical, high-mass-loading conditions.

1 | Introduction

The growing demand for electric vehicles (EVs) and large-scale energy storage systems (ESS) has significantly increased the need for lithium-ion batteries (LIBs) that offer both high energy density and fast-charging capability [1–3]. To meet these requirements, achieving stable charging within tens of minutes has become a critical challenge, demanding integrated progress in material design and electrode architecture.

Among commercial cathode materials [4, 5], olivine-type $LiFePO_4$ (LFP) has achieved widespread commercial adoption owing to its excellent thermal stability, safety, and low production cost [6, 7]. However, the relatively low operating voltage of ~3.4 V

Bonyoung Ku and Lahyeon Jang contributed equally to this work.

(vs. Li^+/Li) limits its energy density, making it less suitable for high-energy and fast-charging applications [8, 9]. To overcome this drawback, Mn-substituted $Li[Mn_xFe_{1-x}]PO_4$ (LMFP) has emerged as a promising olivine-based cathode. The introduction of Mn enables an additional Mn^{2+}/Mn^{3+} redox couple near 4.1 V, enhancing the working voltage while preserving the structural robustness of the LFP framework [10, 11]. In particular, Mn-rich compositions (>0.5 mol Mn) such as $Li[Mn_{0.6}Fe_{0.4}]PO_4$ (LMFP-Mn0.6) strike a practical balance between voltage and capacity, drawing attention as cost-effective, high-voltage cathode candidates for next-generation LIBs [12].

Despite these advantages, Mn-rich LMFP suffers from poor fast-charging performance [13], particularly under high-mass-loading or thick electrode configurations essential for practical cell-level energy density [14]. The low intrinsic electronic conductivity of olivine-type structures, combined with the sluggish Li^+ diffusion kinetics aggravated by Jahn–Teller distortion during the Mn^{2+}/Mn^{3+} redox process, results in increased internal resistance, pronounced polarization, and substantial capacity decay at high charge rates [15, 16]. While conventional strategies such as surface carbon coating and bulk doping have shown partial improvement by enhancing conductivity or stabilizing the crystal lattice, these approaches often come with synthetic complexity, cost, or limited scalability [17–20]. Moreover, excessive doping may destabilize the phase and degrade long-term cycling performance [21].

More importantly, such conductivity-enhancing strategies are generally incompatible with practical thick electrode designs containing ≥95 wt.% active material, where inactive components must be minimized to achieve competitive energy density [22, 23]. As such, approaches that rely heavily on carbon-rich coatings or conductive additive loading become less effective—or even detrimental—under practical high-mass-loading conditions. Therefore, addressing the intrinsic kinetic limitations of Mn-rich LMFP under realistic electrode conditions requires a shift in focus from bulk transport toward interfacial engineering.

In this study, we demonstrate that for Mn-rich LMFP-Mn0.6 cathode under high-mass-loading electrode conditions (95 wt.% active material, 23 mg cm^{-2}, ~3.5 mAh cm^{-2}), fast-charging performance is primarily governed by charge-transfer resistance (R_{ct}) at the cathode–electrolyte interface rather than bulk Li^+ diffusivity. Comparative electrochemical analyses using galvanostatic intermittent titration technique (GITT) and electrochemical impedance spectroscopy (EIS) revealed that the difference in Li^+ diffusivity between room temperature and 45°C is relatively minor. In contrast, a substantial reduction in R_{ct} was observed at elevated temperature, coinciding with improved high-rate capacity retention [24, 25]. These findings indicate that reducing interfacial resistance is critical to enabling fast charging in Mn-rich LMFP systems.

Further investigation of the surface chemistry revealed that accumulation of LiF—an ionically and electronically insulating byproduct formed during electrolyte decomposition—contributes significantly to R_{ct} buildup during cycling [26]. Unlike well-known layered oxide cathodes, including $LiCoO_2$ (LCO) and $Li[Ni_xCo_yMn_z]O_2$ (NCM) based on high electronic and ionic conductivities, where LiF-rich cathode–electrolyte interphase (CEI) layers can be beneficial for interfacial stability [27–29], LMFP-Mn0.6 exhibited severe kinetic hindrance when such LiF layers dominate the CEI [30, 31]. Because LiF is highly resistive, its accumulation is particularly detrimental in intrinsically low-conductivity olivine cathodes (e.g., Mn-rich LMFP) [32], where interfacial charge transport can become the dominant kinetic bottleneck, unlike in layered oxides such as LCO [33] and NCM [34]. This drawback can be further amplified under practical high-mass-loading conditions [14]. While low-rate behavior may not differ markedly from that of low-mass-loading electrodes [35], the accumulation of insulating species (e.g., LiF) within the CEI leads to pronounced interfacial polarization, which becomes more pronounced at high charge rates [36]. As a result, both the rate performance and cycling stability of Mn-rich LMFP cathodes can be adversely affected under practical high-mass-loading conditions. This contrast underscores the importance of tailoring CEI composition specifically for olivine-type systems, where interfacial conductivity is a more critical factor than passivation.

To address the dominant interfacial limitation in Mn-rich LMFP cathodes under high-mass-loading electrode conditions, we engineered the CEI to suppress LiF via a fluoride-scavenging interfacial design, implemented with a model borate-based additive, tris(trimethylsilyl) borate (TMSB). Through first-principles calculation, it was demonstrated that this CEI design strategy utilizes the strong Lewis acidity at the boron center, enabling preferential coordination with anionic species such as F^-. Notably, the B–F bond is thermodynamically stable, suggesting that interfacial fluorine scavenging can effectively capture fluoride ions generated from electrolyte decomposition and thereby suppress the formation of resistive LiF species. As a result, this interfacial engineering strategy yields a thinner, more conductive CEI and mitigates interfacial polarization at high charge rates.

Experimentally, LMFP-Mn0.6 with a LiF-less CEI layer (LiF-less@LMFP) exhibited a substantial reduction in R_{ct} and improved rate capability across a wide current range, compared to LMFP-Mn0.6 with a LiF-rich CEI layer (LiF-rich@LMFP). Under 1C charge conditions, the LiF-less@LMFP delivered a high charge capacity of ~128 mAh g^{-1} and sustained an energy density of approximately ~439 Wh kg^{-1} during discharge, both of which surpass those of the LiF-rich@LMFP (~120 mAh g^{-1} and ~397 Wh kg^{-1}). Especially, even at 5C, it achieved a 158% higher charge capacity compared to the LiF-rich@LMFP. Long-term cycling at 2C further demonstrated enhanced durability, as the LiF-less@LMFP retaining ~87% of its initial capacity after 100 cycles, a significant improvement over the 56% retention observed for the LiF-rich@LMFP.

Operando X-ray diffraction (XRD) and EIS analyses further validated that the LiF-less@LMFP undergoes smaller structural distortion and fewer phase transitions at high charge rates, accompanied by consistently lower interfacial resistance. These results collectively demonstrate that the suppression of resistive interfacial layers, particularly LiF, plays a key role in reducing charge-transfer resistance and thereby unlocking the fast-charging potential of Mn-rich LMFP cathodes for low-cost and high-energy LIBs.

2 | Result and Discussion

2.1 | High-Mass-Loading Mn-Rich $Li[Mn_xFe_{1-x}]PO_4$ (LMFP, x>0.5) Cathode: Structural Characterization and Governing Factor of Fast-Charging Behavior

To improve the energy density of LIBs for practical applications, high-mass-loading electrode designs have become essential [37]. To evaluate the fast-charging performance of the Mn-rich LMFP-Mn0.6 cathodes under such realistic conditions, we fabricated electrodes comprising 95 wt.% active material, with a mass loading of 23 mg cm^{-2} and an areal capacity of ~3.5 mAh cm^{-2}. Cross-sectional Scanning electron microscopy (SEM) analysis of the final electrode showed a dense and uniform structure with a thickness of ~93 μm (Figure S1), and EDS mapping confirmed uniform dispersion of both the LMFP-Mn0.6 components and conductive carbon throughout the electrode (Figure S2). It was also identified that the electrode thickness increased proportionally with the mass loading (Figure S3).

Building upon these morphological observations, the electrode's structural characteristics were further examined through press density and porosity analyses. The electrode exhibited a press density of 2.6 g cm^{-3}, notably higher than the typical value reported for conventional LMFP electrodes (~2.3 g cm^{-3}) [38, 39]. Such densification is expected to enhance the volumetric energy density while mitigating internal resistance. In addition, the porosity estimated from the press density was ~24%, which ensures sufficient electrolyte infiltration and the establishment of favorable ionic transport pathways, while simultaneously maintaining high energy density enabled by the elevated press density [13, 40–42].

The phase purity and crystallinity of LMFP-Mn0.6 active material used in the electrode fabrication were assessed through X-ray diffraction (XRD) analysis, which showed diffraction peaks corresponding exclusively to the orthorhombic olivine structure without any detectable secondary phases or impurities (Figure S4 and Table S1). Rietveld refinement further verified that the refined lattice parameters (a = 10.4063(5) Å, b = 6.0667(3) Å, c = 4.7268(2) Å, V = 298.4116(9) $Å^3$) are in close agreement with previously reported LMFP structures [35, 43]. Moreover, the particles exhibited a uniform morphology with an average diameter of ~0.25 μm (Figure S5 and S6), and SEM-based energy-dispersive X-ray spectroscopy (EDS) mapping confirmed homogeneous elemental distribution (Figure S7).

At room temperature, the LMFP-Mn0.6 electrode delivered a charge capacity of ~156.3 mAh g^{-1} at 0.1C (1C = 160 mA g^{-1}) under the high-mass-loading conditions (Figure 1a). However, under fast-charging conditions (2C), the capacity sharply declined to 96.83 mAh g^{-1}, corresponding to only ~62% of the 0.1C value (Figure 1b), clearly indicating limited rate capability at ambient temperature. Interestingly, when tested at high temperature (45°C), the charge capacity increased to ~156.6 mAh g^{-1} at 0.1C and ~107.9 mAh g^{-1} at 2C, corresponding to a negligible change (~0.17%) at low rate and a significant 11.4% improvement at high rate compared to room temperature (Figure 1a,b). Notably, the electrode also exhibited a considerably lower overpotential at 2C under the high temperature, indicating reduced polarization and improved reaction kinetics. This observation is consistent with previous reports on LMFP-based cathodes, where enhanced power performance at elevated temperatures has been attributed to improved interfacial kinetics.

To elucidate the origin of improved fast-charging performance of LMFP-Mn0.6 at elevated temperature, we performed a comparative analysis of the temperature dependence of two key factors known to critically influence rate capability: bulk Li^+ diffusion and interfacial charge-transfer resistance.

If bulk Li^+ diffusion were the rate-limiting step, a significant increase in the Li^+ diffusivity (D_{Li+}) would be expected upon temperature elevation. To evaluate the influence of temperature on D_{Li+}, GITT measurements were conducted based on the method proposed by Weppner and Huggins [44, 45]. Assuming diffusion follows Fick's second law, D_{Li+} was calculated using Equation (1):

$$D_{Li+} = \frac{4}{\pi\tau}\left(\frac{mV}{MS}\right)^2\left(\frac{\Delta E_s}{\Delta E_t}\right)^2, \left(\tau \ll \frac{L^2}{D_{Li+}}\right)^2 \quad (1)$$

here, τ is the duration of constant current application, m denotes the mass of the active material, V is the molar volume of the cathode, M corresponds to the molar mass of the cathode, S indicates the contact surface area between the electrode and electrolyte, ΔE_s is the voltage change observed during a single step, and ΔE_t refers to the total voltage change under the applied constant current conditions.

At room temperature under a 0.1C rate, GITT measurements revealed D_{Li+} values of the LMFP-Mn0.6 to be ~1.68×10^{-7} cm^2 s^{-1} in the Fe redox region and ~1.03×10^{-9} cm^2 s^{-1} in the Mn redox region (Figure 1c). Importantly, similar values were obtained at elevated temperature (45°C), as shown in Figure 1d, indicating that D_{Li+} is relatively insensitive to thermal activation. This observation indicates that bulk Li^+ diffusion does not dominate the rate performance under these conditions.

In contrast, EIS analysis revealed that the R_{ct} is highly sensitive to temperature under fast-charging conditions. During 2C charging, the LMFP-Mn0.6 cell exhibited a notably lower R_{ct} at high temperature than at room temperature, indicating improved interfacial reaction kinetics at elevated temperature. Importantly, the R_{ct} measured after full charging was ~14.79 Ω at room temperature and was significantly reduced to ~6.74 Ω at high temperature, as shown in the Nyquist plots and fitted equivalent circuit (Figure 1e,f), corresponding to only ~46% of the room temperature value [46]. This substantial reduction in R_{ct} implies that the difference in fast-charging performance between room temperature and high temperature is primarily governed by interfacial charge-transfer resistance.

To clarify the characteristic redox couples of the LMFP cathode, cyclic voltammetry (CV) was performed at room temperature with a scan rate of 0.1 mV s^{-1} (Figure S8). As shown in the CV curves, distinct anodic peaks appeared at approximately 3.59 and 4.18 V during the anodic scan. During the subsequent cathodic scan at the same rate, pronounced cathodic peaks were observed

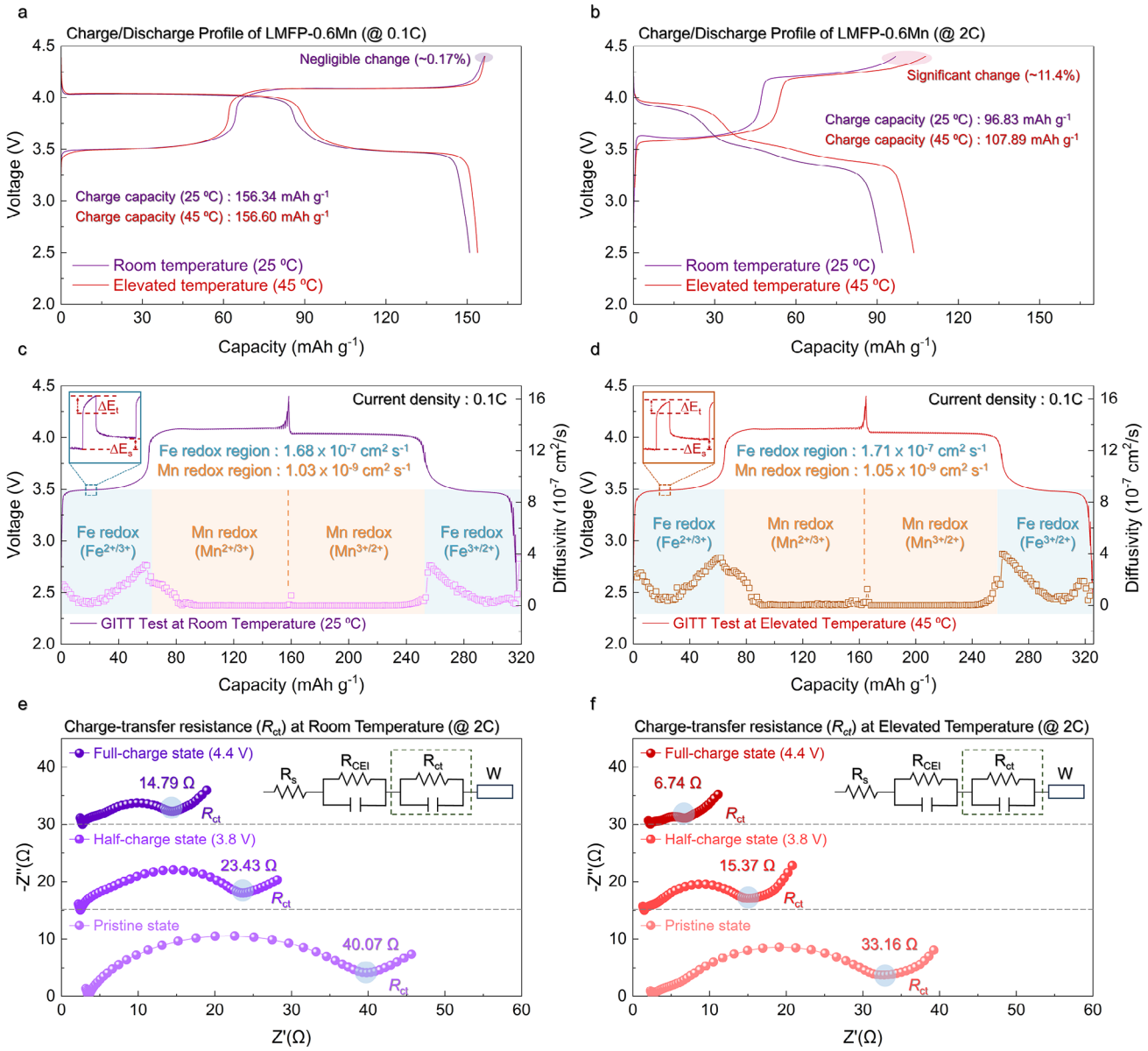

FIGURE 1 | Initial charge/discharge profiles of $Li[Mn_{0.6}Fe_{0.4}]PO_4$ cathode under room temperature and elevated temperature at (a) 0.1C and (b) 2C. GITT results obtained at a 0.1C under (c) room temperature conditions and (d) elevated temperature conditions. EIS results measured after full charging at a 2C current rate at (e) room temperature and (f) elevated temperature.

at around 3.41 and 3.93 V. These results confirm that the Fe^{2+}/Fe^{3+} redox couple occurs at ~3.59/3.41 V, whereas the Mn^{2+}/Mn^{3+} redox couple occurs at ~4.18/3.93 V, thereby identifying the characteristic redox couples of the LMFP cathode.

These findings strongly support that, in fast-charging Mn-rich LMFP systems, the principal bottleneck lies not in bulk diffusion but in interfacial reaction kinetics, which becomes further aggravated under high-mass-loading conditions. Consequently, at room temperature, where interfacial kinetics are not sufficiently activated, performance degradation becomes more pronounced. Therefore, identifying and overcoming the fundamental interfacial limitations are essential to unlocking the fast-charging potential of Mn-rich LMFP cathodes.

2.2 | Interfacial Engineering Strategy for Suppressing the Formation of Insulating LiF and Enhancing Fast-Charging Performance of Mn-Rich LMFP

As previously mentioned, the fast-charging performance of Mn-rich LMFP-Mn0.6 under high-mass-loading conditions is dominantly limited by the R_{ct}, rather than bulk Li^+ diffusion. This finding underscores the importance of controlling the interfacial environment, particularly by preventing the formation of resistive surface species that hinder ion transport.

One of the key contributors to interfacial resistance is the formation of insulating LiF at the interface between cathode and

electrolyte, especially when using conventional $LiPF6^-$ containing carbonate electrolytes [47]. In these systems, LiF formation primarily originates from the generation of reactive F^- species from the decomposition of $LiPF_6$. While such insulating LiF may offer interfacial stability in layered oxide cathodes, such as NCM, $LiCoO_2$, etc., with high intrinsic electrical conductivity [27], they can be highly detrimental in Mn-rich LMFP-based systems, which already suffer from limited electronic conductivity. The presence of the insulating LiF phase at the interface can severely impede Li^+ transport, particularly under fast-charging and high-thickness electrode conditions.

To mitigate this issue, we adopted an interfacial engineering strategy aimed at the formation of a LiF-less interface on the surface of Mn-rich LMFP particles. The underlying approach involves selectively scavenging reactive F^- species before they form resistive deposits on the cathode surface. To achieve this, TMSB was employed to capture fluorine species through preferential coordination reactions. As shown in Figure 2a, DFT calculations revealed that the boron center in TMSB exhibits strong Lewis acidity, leading to the preferential binding of F^- over Li^+. The calculated binding energy of F^- to TMSB is lower than that for LiF formation, indicating that F^- is thermodynamically more favorable to interact with TMSB rather than to form LiF under the same conditions. Therefore, the early formation of resistive LiF deposits can be successfully suppressed during the formation of the initial CEI layer, promoting the development of a LiF-less interphase that minimizes electronic and ionic blocking at the cathode–electrolyte interface. In addition, the relatively high oxidation potential of TMSB, which lies within the electrochemical stability window of the carbonate-based electrolyte (Figure S9), implies that TMSB remains electrochemically stable during the early stages of charging and begins to oxidize at the higher voltage regions. This suggests that TMSB initially adsorbs the fluorine species through spontaneous Lewis acid–base interactions and subsequently participates in CEI formation.

To experimentally validate the influence of LiF suppression on interfacial behavior, electrochemical tests were performed on two types of LIB cells: LMFP-Mn0.6 with a LiF-rich CEI layer (LiF-rich@LMFP) and LMFP-Mn0.6 with a LiF-less CEI layer (LiF-less@LMFP). The LiF-less CEI condition was achieved by introducing 1 wt.% TMSB as an electrolyte additive. At a current density of 1C, LiF-rich@LMFP exhibited a charge capacity of ~120.3 mAh g^{-1} and a discharge capacity of ~109.6 mAh g^{-1} (Figure 2b). In contrast, LiF-less@LMFP demonstrated a higher charge capacity of ~128.3 mAh g^{-1} and a discharge capacity of ~120.1 mAh g^{-1} (Figure 2c). Under fast-charging conditions, performance divergence became more evident. At 5C, LiF-less@LMFP maintained a charge capacity of ~65.6 mAh g^{-1} and a discharge capacity of ~62.5 mAh g^{-1}, approximately 1.58 times higher than those of LiF-rich@LMFP. Moreover, LiF-less@LMFP consistently exhibited lower overpotentials during charging across all current rates compared to LiF-rich@LMFP, indicating improved Li^+ transport across the interface (Figure 2d; Figure S10). These enhancements are attributed to the suppression of insulating LiF formation, rather than simple CEI thickening or decomposition effects.

To confirm the specificity of this LiF-suppression effect by application of TMSB, a comparative test was conducted using 1 wt.% lithium bis(oxalate)borate (LiBOB) for CEI-controlling (denoted as LiBOB@LMFP). Although LiBOB also contains a boron center like TMSB, it lacks the strong Lewis acidity required for effective F^- capture. DFT calculations confirmed that F^- binding to LiBOB is thermodynamically unfavorable compared to LiF formation, in contrast to TMSB, which exhibits preferential F^- binding due to its electron-deficient boron center (Figure S11). Accordingly, LiBOB@LMFP showed degraded electrochemical performance across all current densities compared to both LiF-rich@LMFP and LiF-less@LMFP (Figure S12), highlighting that not all boron-containing additives are equally effective. These results reinforce that suppression of the LiF formation in the CEI layer requires not simple control of chemical composition, but specific molecular features—such as strong Lewis acidity—for effective F^- scavenging.

To verify whether this behavior is also maintained under elevated-temperature conditions, we performed electrochemical tests on LiF-rich@LMFP and LiF-less@LMFP under identical conditions at elevated temperature. As a result, at a low rate of 0.1C, the charge capacities of the two electrodes were nearly identical; however, a clear performance divergence emerged under fast-charging conditions (Figures S13 and S14). In particular, at 5C, LiF-less@LMFP delivered 1.32 times higher charge capacity than LiF-rich@LMFP. These results indicate that the LiF-suppression strategy can further enhance fast-charging performance even at elevated temperatures.

We also examined whether this LiF-suppression strategy can be successfully extended to compositions with higher Mn content (Mn > 0.6). To this end, $LiMn_{0.8}Fe_{0.2}PO_4$ (LMFP-Mn0.8) was synthesized, showing a phase-pure product without detectable impurities and an average particle size of ~0.23 μm (Figures S15 and S16 and Table S2). Electrochemical tests were then conducted for LMFP-Mn0.8 with a LiF-rich CEI layer (LiF-rich@LMFP-Mn0.8) and LMFP-Mn0.8 with a LiF-less CEI layer (LiF-less@LMFP-Mn0.8). Similar to the LMFP-Mn0.6, the charge capacities at 0.1C were nearly identical, whereas a pronounced difference appeared under fast-charging conditions (Figures S17 and S18). Notably, at 3C, LiF-less@LMFP-Mn0.8 exhibited 1.44 times higher charge capacity than LiF-rich@LMFP-Mn0.8. This demonstrates that the LiF-suppression strategy remains effective for improving fast-charging performance even in Mn-rich compositions.

To gain mechanistic insight, we returned to the representative Mn0.6 composition and examined the interfacial resistance by Direct Current-Internal Resistance (DC-IR) measurements [48, 49]. After the first activation cycle, the cell was charged at a low current density of 0.1C for 1 h. Following this, the cell was rested for 10 min and then rapidly charged for 30 s at 2C. DC-IR was calculated based on the voltage change over current (ΔV/I) during this experiment. Afterward, the cell was rested for another 10 min, and charging was resumed at 0.1C. Additional DC-IR tests were performed until the cell was fully charged. Through these experiments, the average DC-IR values in the Fe and Mn redox regions were obtained. As shown in Figure 2e,f, it was verified that LiF-rich@LMFP exhibited a ΔDC-IR of ~48.52 mΩ in the Fe redox region and ~89.14 mΩ in the Mn redox region. In contrast, LiF-less@LMFP demonstrated significantly lower values of ~35.71 and ~77.43 mΩ in the Fe and

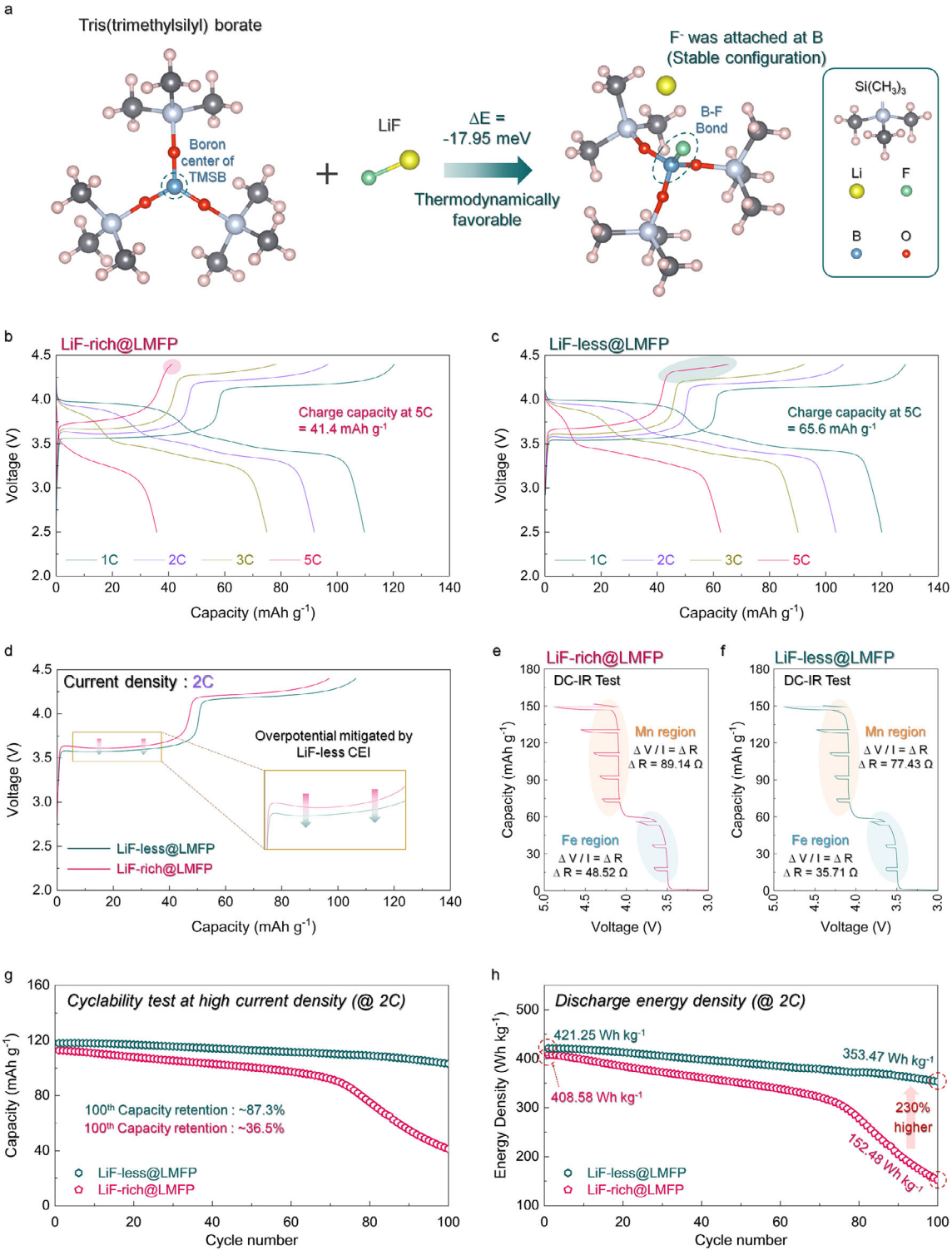

FIGURE 2 | (a) First-principles calculation of the LiF-suppression mechanism via TMSB. Charge/discharge curves of the (b) LiF-rich@LMFP and (c) LiF-less@LMFP in the voltage range of 2.5–4.4 V (vs. Li/Li^+) at various current rates. (d) Comparison of the charging profiles of LiF-rich@LMFP and LiF-less@LMFP at a 2C. DC-IR test results of (e) LiF-rich@LMFP and (f) LiF-less@LMFP, during the charging process at a 2C. (g) Cycling performance and (h) discharge energy density of LiF-less@LMFP and LiF-rich@LMFP over 100 cycles at a 2C.

Mn redox regions, respectively. These results confirm that LiF-less@LMFP can deliver the enhanced charge-transfer kinetics and fast-charging performance via the formation of a LiF-less CEI layer.

Moreover, to assess the structural stability of LiF-less@LMFP, long-term cycling under fast-charging conditions was conducted at 2C with constant current-constant voltage (CC-CV) charging conditions (Figure 2g) [50]. LiF-less@LMFP electrode retained

~87.3% of its initial capacity after 100 cycles, while LiF-rich@LMFP underwent rapid degradation, retaining only ~36.5% of its capacity over the same period. The average discharge voltage of LiF-less@LMFP decreased by ~2.18 mV per cycle, while LiF-rich@LMFP showed a decrease of ~2.89 mV per cycle (Figure S19). Furthermore, after 100 cycles, LiF-less@LMFP exhibited 2.3-times higher energy density compared to LiF-rich@LMFP (Figure 2h). Additionally, SEM imaging after 100 cycles revealed that, while LiF-less@LMFP retained uniform particle structure, cracks appeared in the particles of LiF-rich@LMFP (Figure S20). In addition, to confirm structural stability, cyclability was also examined under full-cell conditions with the 2C charging process, and LiF-less@LMFP retained ~71.47% after 700 cycles, whereas LiF-rich@LMFP retained only ~58.98% (Figure S21). Moreover, LiF-less@LMFP exhibited a 123% higher energy density than LiF-rich@LMFP after 700 cycles (Figure S22). To further evaluate the structural stability under the elevated-temperature condition, we additionally conducted long-term cycling tests under the same fast-charging protocol. Under elevated-temperature conditions, degradation was accelerated compared to room temperature: LiF-rich@LMFP exhibited a capacity retention of only 36.9% after 70 cycles, whereas LiF-less@LMFP maintained 90.5% after 70 cycles (Figure S23). In addition, for the Mn-enriched LMFP-Mn0.8 composition, the increased Mn content led to a pronounced deterioration in structural stability. As a result, LiF-rich@LMFP-Mn0.8 showed a low capacity retention of 37.5% after 70 cycles. In contrast, LiF-less@LMFP-Mn0.8 retained 84.0% of its capacity after 70 cycles (Figure S24).

These results demonstrate that suppressing resistive LiF formation at the interface enables the formation of a conductive and stable CEI layer, thereby significantly enhancing both the fast-charging performance and long-term durability of high-mass-loading Mn-rich LMFP cathodes.

2.3 | Direct Evidence for Suppressed LiF Formation in the CEI layer of LiF-less@LMFP

To elucidate the origin of improved electrochemical performance in LiF-less@LMFP, surface-sensitive characterizations were conducted to investigate the CEI composition and morphology. X-ray photoelectron spectroscopy (XPS) measurements were performed at the fully charged state to identify surface species generated through interfacial reactions during the charging process. The F 1*s* XPS spectrum of LiF-rich@LMFP exhibited a strong peak at 685.5 eV [51], corresponding to Li–F bonding, which accounted for 26.20% of the total area (Figure 3a) [52]. These results confirm the significant accumulation of LiF-related species on the surface of LiF-rich@LMFP. In contrast, LiF-less@LMFP showed a markedly reduced Li–F signal, occupying only 1.81% of the total area, suggesting effective suppression of interfacial LiF formation.

Moreover, to examine this process more closely, F 1*s* XPS was further performed at various states (Figure S25). During charging, LiF-rich@LMFP exhibited a continuous increase in the Li–F bonding signal, indicating progressive Li–F species formation, whereas LiF-less@LMFP maintained a negligible Li–F bonding signal throughout charging. Notably, this contrast remained evident even after 100 cycles (Figure S26). For LiF-rich@LMFP, the Li–F bonding signal increased substantially, whereas LiF-less@LMFP showed a much lower contribution, demonstrating that the LiF-suppression strategy remains effective upon prolonged cycling.

To verify whether the LiF-suppression strategy is maintained under elevated-temperature conditions, XPS measurements were performed at the fully charged state after charging at 45°C. Under these conditions, LiF-rich@LMFP exhibited a pronounced Li–F bonding signal, whereas only a negligible contribution was observed for LiF-less@LMFP, demonstrating that the LiF-suppression effect is effectively preserved even at elevated temperature (Figure S27). Furthermore, this difference remained evident even after 70 cycles at elevated temperature. In LiF-rich@LMFP, the Li–F signal increased to as much as 63.11% of the total area, whereas LiF-less@LMFP showed a Li–F signal of ~13.60% (Figure S28). Although degradation progressed more under elevated temperature conditions than at room temperature, these results confirm that the LiF-suppression strategy is still effectively maintained even after cycling at elevated temperature, leading to a significantly reduced Li–F signal.

Furthermore, to confirm whether this strategy remains effective for the Mn-enriched LMFP-Mn0.8 composition, XPS measurements were performed at the fully charged state. As a result, LiF-rich@LMFP-Mn0.8 exhibited a strong Li–F bonding signal accounting for 27.67% of the total area, whereas LiF-less@LMFP-Mn0.8 showed only ~2.11%, demonstrating that the effect is successfully maintained even under increased Mn content (Figure S29).

Additional insights were obtained from the O 1*s* XPS spectra. A distinct B–O peak at 531.96 eV was observed in LiF-less@LMFP, indicating the incorporation of boron-containing species into the CEI layer (Figure 3b) [53, 54]. Also, to examine whether the LiF-suppression also mitigates Li plating on the anode, graphite electrodes were recovered from LiF-rich@LMFP||graphite and LiF-less@LMFP||graphite full cells and analyzed by SEM and XPS. In the graphite anode of the LiF-rich@LMFP-based full cell, plating-related deposits were observed after the first cycle, and distinct dendritic features appeared after 100 cycles (Figure S30). In contrast, such deposits were largely suppressed in the graphite anode of the LiF-less@LMFP-based full cell, and no obvious plating features were observed even after 100 cycles. Consistently, after 100 cycles, Li 1*s* XPS showed that the Li metal component fraction (associated with Li plating) decreased from 45.27% (graphite anode of the LiF-rich@LMFP-based full cell) to 12.56% (graphite anode of the LiF-less@LMFP-based full cell, confirming that Li plating was substantially mitigated (Figure S31) [55]. Overall, suppressing LiF formation in the cathode CEI reduces R_{ct} and polarization, thereby improving cathode kinetics and providing an additional, indirect benefit by alleviating anode-side dendritic Li plating and SEI degradation under the same fast-charging conditions.

Moreover, solution nuclear magnetic resonance (NMR) shows that LiF-rich@LMFP exhibits ^{19}F resonances near −156 and −193 ppm associated with HF/F^- in the fully charged state [56], whereas in LiF-less@LMFP these features fall below the detection limit and are replaced by abundant signals between −147 and −160 ppm attributable to borate-type B–F species

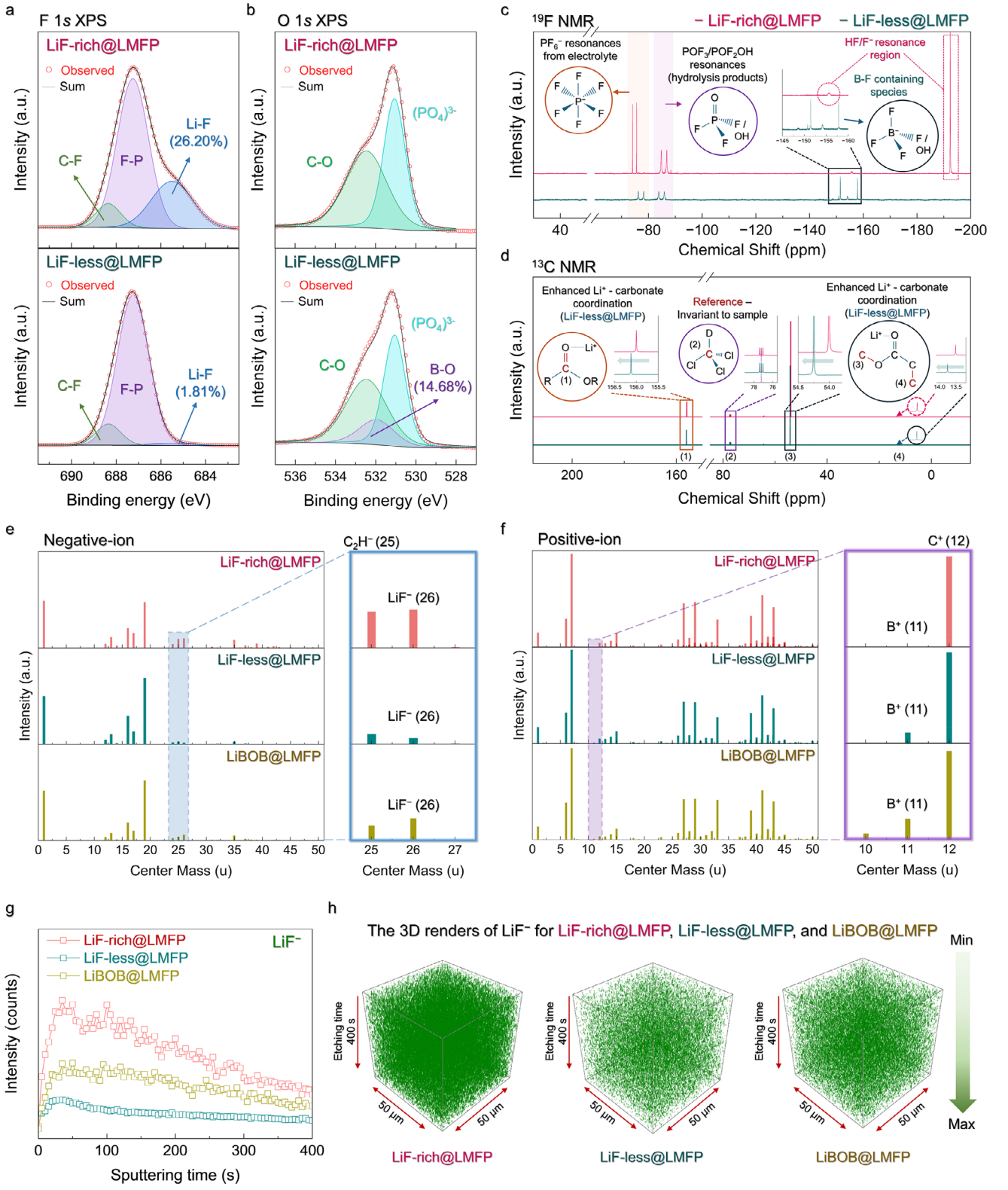

FIGURE 3 | (a) F 1*s* XPS spectra of LiF-rich@LMFP and LiF-less@LMFP. (b) O 1*s* XPS spectra of LiF-rich@LMFP and LiF-less@LMFP. (c) ^{19}F NMR spectra of LiF-rich@LMFP and LiF-less@LMFP, showing PF_6^-, hydrolysis-derived POF_3/POF_2OH, HF/F^-, and B–F containing species. (d) ^{13}C NMR spectra of LiF-rich@LMFP and LiF-less@LMFP, indicating enhanced Li^+ coordination through chemical shift variations of carbonyl, solvent, alkoxy, and methyl carbons. ToF-SIMS surface analysis of LiF-rich@LMFP, LiF-less@LMFP, and LiBOB@LMFP in (e) negative-ion and (f) positive-ion detection mode. (g) 3D ToF-SIMS depth profile of LiF^- species and (h) visualization of the depth profiling results.

(often split by the natural $^{10}B/^{11}B$ isotopes) (Figure 3c) [57]. Consistently, ^{11}B NMR detects no detectable boron signal in LiF-rich@LMFP under identical conditions, while LiF-less@LMFP displays a resonance characteristic of four-coordinate (tetrahedral) boron, corroborating the formation of borate/fluoroborate species (Figure S32) [58]. In addition, LiF-less@LMFP displays downfield shifts in $^{1}H/^{13}C$ ($\delta \approx 156, 54, 13.5$ ppm) and ^{7}Li together with a pronounced narrowing of the ^{7}Li line (Figure 3d; Figures S33 and S34) [59–61]. These spectral observations indicate that TMSB captures fluorine-containing species, thereby suppressing LiF formation within the CEI layer and stabilizing the interfacial chemistry of the Mn-rich LMFP.

This result is further corroborated by time-of-flight secondary ion mass spectrometry (ToF-SIMS). In the negative ion detection mode, the LiF^- signal ($m/z \approx 26$) was markedly reduced in LiF-less@LMFP compared to LiF-rich@LMFP and LiBOB@LMFP (Figure 3e) [62]. When considered alongside the B–O XPS analysis in Figure 3b, a consistent trend is observed. LiF-less@LMFP, which exhibited the weakest B–O signal, also showed the lowest LiF accumulation. These results suggest that suppressing F^--driven compound formation, rather than simply generating a B-rich CEI, plays a critical role in enhancing interfacial properties.

Positive ion detection in ToF-SIMS further clarified the role of additive-derived species. Boron signals ($m/z \approx 11$) were observed in both LiF-less@LMFP and LiBOB@LMFP but were absent in LiF-rich@LMFP (Figure 3f). Notably, the boron signal intensity was weaker in LiF-less@LMFP than in LiBOB@LMFP, despite its superior electrochemical performance. Three-dimensional ToF-SIMS depth profiling further visualized these differences. Among the three samples, LiF-less@LMFP exhibited the lowest LiF intensity across the interphase region (Figure 3g,h). These results reinforce that effective suppression of insulating LiF formation within the CEI layer is crucial for lowering interfacial resistance and enabling fast-charging performance in Mn-rich LMFP cathodes.

Additionally, to examine whether the performance improvement could be driven by non-F-containing species, carbonate-based decomposition products and organic fragments in the CEI were analyzed using ToF-SIMS (Figure S35). The signal intensities of LiF, organic species, and carbonate-based species detected in LiF-rich@LMFP and LiF-less@LMFP were normalized by the total ion counts and quantitatively compared using the integrated yield. As a result, a LiF^- specie showed a pronounced significant decrease of 60.1%, respectively, whereas negligible changes were observed for organic fragments (e.g., C_2HO^-, CHO_2^-) and carbonate-based species (e.g., CO^-, CO_2^-, $LiCO_3^-$, $Li_2CO_3^-$) (Figure S36). Moreover, this trend was further corroborated by the 3D rendering results, which visualized these differences more clearly (Figure S37). Taken together, these results indicate that the enhanced fast-charging performance of Mn-rich LMFP cathodes is primarily associated with effective suppression of insulating LiF, rather than changes in organic or carbonate-based CEI components.

To directly observe the CEI morphology, high-resolution transmission electron microscopy (HR-TEM) was conducted after the first activation cycle. The LiF-rich@LMFP sample displayed a thick (~5 nm) and non-uniform CEI layer, while LiF-less@LMFP showed a thinner and more uniform layer (~2 nm) (Figure S38). After 100 cycles, the CEI layer of LiF-rich@LMFP exhibited further thickening and structural inhomogeneity, whereas LiF-less@LMFP maintained a stable and conformal CEI layer of ~3 nm thickness (Figure S39). These observations suggest that suppressing the formation of resistive LiF helps maintain a thinner and more stable interfacial layer, which in turn facilitates long-term electrochemical stability.

2.4 | Operando XRD and EIS Study of LiF-Less CEI Layer Enabling Fast-Charging Mn-Rich LMFP Cathodes

To investigate how interfacial LiF-suppression affects Li^+ transport and structural stability under fast-charging conditions, a series of comprehensive *operando* experiments was conducted. First, *operando* XRD analysis was performed to analyze lattice parameter changes during cycling. Under the low-rate condition (0.1C), both LiF-rich@LMFP and LiF-less@LMFP exhibited solid-solution behavior in the early stages of charging, as evidenced by the gradual shift of the various XRD peaks. As Li^+ deintercalation progressed, a two-phase reaction emerged, accompanied by the formation of a distinct $Mn_{0.6}Fe_{0.4}PO_4$ (Li_0MFP) phase (Figure 4a; Figure S40) [63].

Detailed analysis of lattice parameter changes in LiF-less@LMFP revealed that the *a*-lattice and unit cell volume continuously decreased during Li^+ deintercalation. Until the solid-solution behavior ended during charging, the *a*-lattice exhibited a change rate of ~2.90%, and the volume showed a change rate of ~3.14% (Figure 4b). When the solid-solution behavior ended and the two-phase region initiated, the lattice parameter and volume of the Li_0MFP phase were measured and compared to those of the solid-solution phase within the LiF-less@LMFP structure at the same state-of-charge (SOC). The *a*-lattice parameter and volume of the Li_0MFP phase differed by ~3.41% and ~4.66%, respectively, from those of the solid-solution phase at this point. Upon subsequent discharge, Li^+ was re-intercalated into the structure, and the original lattice parameters were nearly restored, indicating good reversibility. However, LiF-rich@LMFP exhibited not only larger variation in the *a*-lattice (~3.11 %) and volume (~3.41 %) during Li^+ deintercalation but also incomplete recovery of the solid-solution lattice parameters upon full discharge (Figure S41). These results suggest reduced structural reversibility in LiF-rich@LMFP during charge/discharge compared to LiF-less@LMFP, which contributes to the fast-charging capability, rate performance, and cycling stability of LiF-less@LMFP.

To assess how this behavior changes under high-rate conditions, *operando* XRD tests were conducted at a 1C rate. In both samples, a continuous solid-solution reaction dominated without clear two-phase transitions (Figure 4c,d), consistent with rate-dependent phase evolution in LMFP. However, a different behavior was observed in LiF-rich@LMFP compared to LiF-less@LMFP. In LiF-rich@LMFP, when some Li^+ was deintercalated, a slight structural distortion occurred at the XRD peak corresponding to (211) plane. Additionally, at full charge, the peak showed a slight break, and the intensity of the

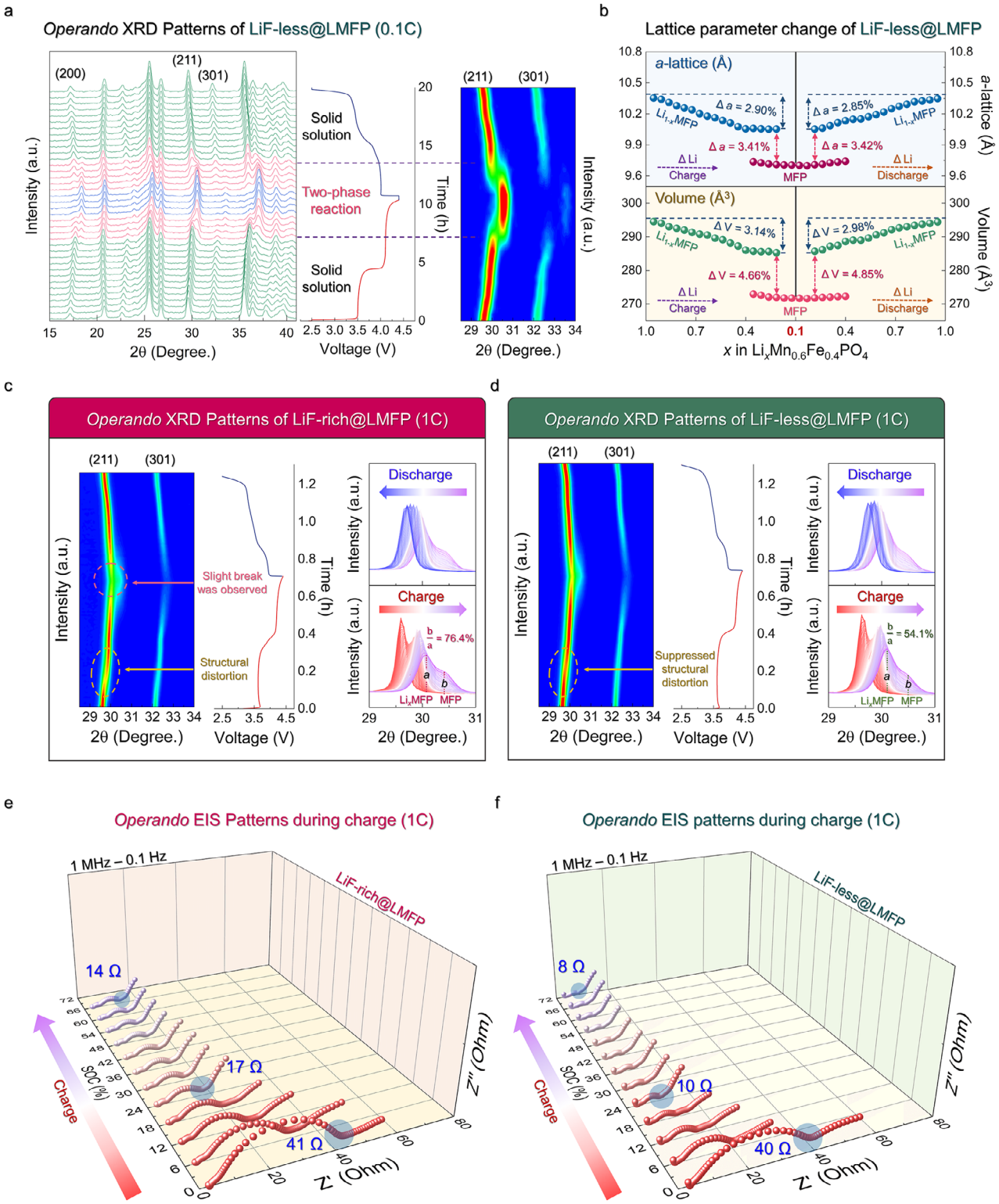

FIGURE 4 | (a) *Operando* XRD patterns, charge/discharge profile, and 2D contour image of LiF-less@LMFP measured at a current rate of 0.1C. (b) Changes in the *a*-lattice parameter and unit cell volume of LiF-less@LMFP during charge/discharge. *Operando* XRD results obtained at a 1C rate for (c) LiF-rich@LMFP and (d) LiF-less@LMFP. *Operando* EIS measurements conducted during the charging process at a 1C rate for (e) LiF-rich@LMFP and (f) LiF-less@LMFP.

Li0MFP phase was nearly 76.4% of the intensity corresponding to the solid-solution phase. In contrast, LiF-less@LMFP exhibited negligible structural distortion during Li^+ deintercalation, and at full charge, the peak remained continuous. Moreover, the intensity corresponding to the Li_0MFP phase was about 54.1% of the intensity for the solid-solution phase, showing a reduced two-phase reaction compared to LiF-rich@LMFP. These findings indicate that suppressing interfacial LiF-formation is essential for maintaining the structural integrity of Mn-rich LMFP under fast-charging conditions.

To directly evaluate the impact of LiF-suppression on interfacial resistance, *operando* EIS measurements were carried out during charging at a rate of 1C (Figure 4e,f). The R_{ct} was monitored at 6% intervals of SOC after the formation of the CEI. At SOC 0%, both LiF-rich@LMFP and LiF-less@LMFP exhibited an R_{ct} of approximately 40 Ω. As charging progressed, the R_{ct} values of both samples gradually decreased, consistent with trends reported for olivine-type cathodes [64]. However, LiF-less@LMFP consistently maintained lower R_{ct} values than LiF-rich@LMFP throughout the entire charging process. In particular, at full charge, LiF-rich@LMFP showed an R_{ct} of approximately 14 Ω, whereas LiF-less@LMFP maintained a significantly lower value of about 8 Ω. This nearly 1.75-fold difference indicates that the LiF-suppressed CEI formed in LiF-less@LMFP more effectively reduces interfacial resistance and facilitates Li^+ transport. Combined with the *operando* XRD results, these findings support that interfacial LiF suppression is essential for achieving stable and efficient Li^+ insertion/extraction under high-rate operation in Mn-rich LMFP cathodes.

3 | Conclusion

As summarized in Figure 5, suppressing the formation of electronically and ionically insulating LiF plays a crucial role in enhancing the fast-charging performance of Mn-rich LMFP cathodes, which inherently suffer from low electronic conductivity and sluggish Li^+ diffusion kinetics aggravated by Jahn–Teller distortion during the Mn^{2+}/Mn^{3+} redox process. Effective interfacial engineering that minimizes LiF accumulation at the CEI layer facilitates rapid Li^+ transport and mitigates charge-transfer resistance, thereby improving overall electrochemical kinetics. As a result, LiF-less@LMFP exhibits superior fast-charging performance, enhanced rate capability, and stable cyclability even under practical high-mass-loading conditions (areal capacity of 3.5 mAh cm^{-2}), compared to LiF-rich@LMFP. Notably, at the high current rate of 5C, the discharge capacity of LiF-less@LMFP is 1.6 times higher than that of LiF-rich@LMFP, accompanied by consistently lower charging overpotentials across all current rates. Detailed surface analyses using XPS, NMR, ToF-SIMS, and HR-TEM clearly identified the accumulation of LiF within the CEI, which acts as the primary factor limiting the fast-charging performance of Mn-rich LMFP cathodes. *Operando* XRD and EIS analyses further demonstrated that suppressing LiF formation preserves a robust single-phase reaction pathway in the Mn-rich LMFP cathode and minimizes interfacial impedance throughout cycling. These insights establish that controlling surface exchange kinetics via interfacial engineering is essential for unlocking the full potential of Mn-rich olivine cathodes, providing a clear design strategy for practical, high-energy, and fast-charging LIBs.

4 | Experimental Section

4.1 | Preparation of Electrolyte Samples

The base electrolyte used in this study was composed of 1.2 M $LiPF_6$ dissolved in a mixture of EC:EMC:DMC in a 2:4:4 volume ratio. Inside an argon-filled glovebox, 1 wt.% of tris(trimethylsilyl)borate (TMSB, purity ≥ 99%, Sigma–Aldrich) was added to the electrolyte, and the solution was stirred at 60°C and 100 rpm for 72 h. After mixing, the solution was left undisturbed for two days to ensure stabilization. For comparison, a sample containing lithium bis(oxalato)borate (LiBOB, purity ≥ 99%) was prepared under the same conditions.

4.2 | Electrochemical Characterization

To fabricate electrodes, the active material ($Li[Mn_{0.6}Fe_{0.4}]PO_4$), conductive carbon, and a PVdF binder were mixed in a weight ratio of 95:2:3. using an anhydrous N-methyl-2-pyrrolidone (NMP) solvent. The resulting slurry was uniformly coated onto carbon-coated aluminum foil using the doctor-blade technique and subsequently dried at 100°C for approximately 5 h. The fabricated electrodes exhibited an areal loading of 23 mg cm^{-2}. The electrode thickness was determined from cross-sectional SEM analysis. The corresponding press density was calculated using $\rho = M_a/S \times L$ where M_a is the mass of active LMFP-Mn0.6, S is the electrode area, and L is the thickness obtained from SEM. The porosity (P) was then obtained using $p = 1 - P_{electrode}/P_{true}$, with P_{true} representing the weighted average density of all solid components in the electrode formulation. Coin-type half cells (CR2032) were assembled in an argon atmosphere using lithium metal as both reference and counter electrodes, the prepared LMFP cathode, a polyethylene separator, and the electrolyte containing 1 wt.% TMSB. All assembly steps were carried out in a glovebox (H_2O, O_2<0.1 ppm). Charge/discharge cycling was performed at current rates of 0.1C–5C within a voltage range of 2.5–4.4 V using a WonATech WBCS3000 battery tester. After one formation cycle at 0.1C, long-term cycling was evaluated at a fixed rate of 2C. To minimize polarization, the upper voltage limit was held until the current dropped to 0.33C before discharge.

4.3 | Electrochemical Impedance Spectroscopy

Operando EIS tests were carried out using a ZIVE MP2F system (WonATech) during the charging process at a 1C rate. Impedance measurements were taken at every 6% increment in the state of charge (SOC) from 0% to 72%, applying a 10 mV AC signal across a frequency range of 1 MHz–100 mHz. Prior to each measurement, the cells were held until the voltage reached a stable value.

4.4 | X-Ray Diffraction

The crystal structure of the $Li[Mn_{0.6}Fe_{0.4}]PO_4$ cathode was analyzed using a PANalytical Empyrean diffractometer with Mo Kα

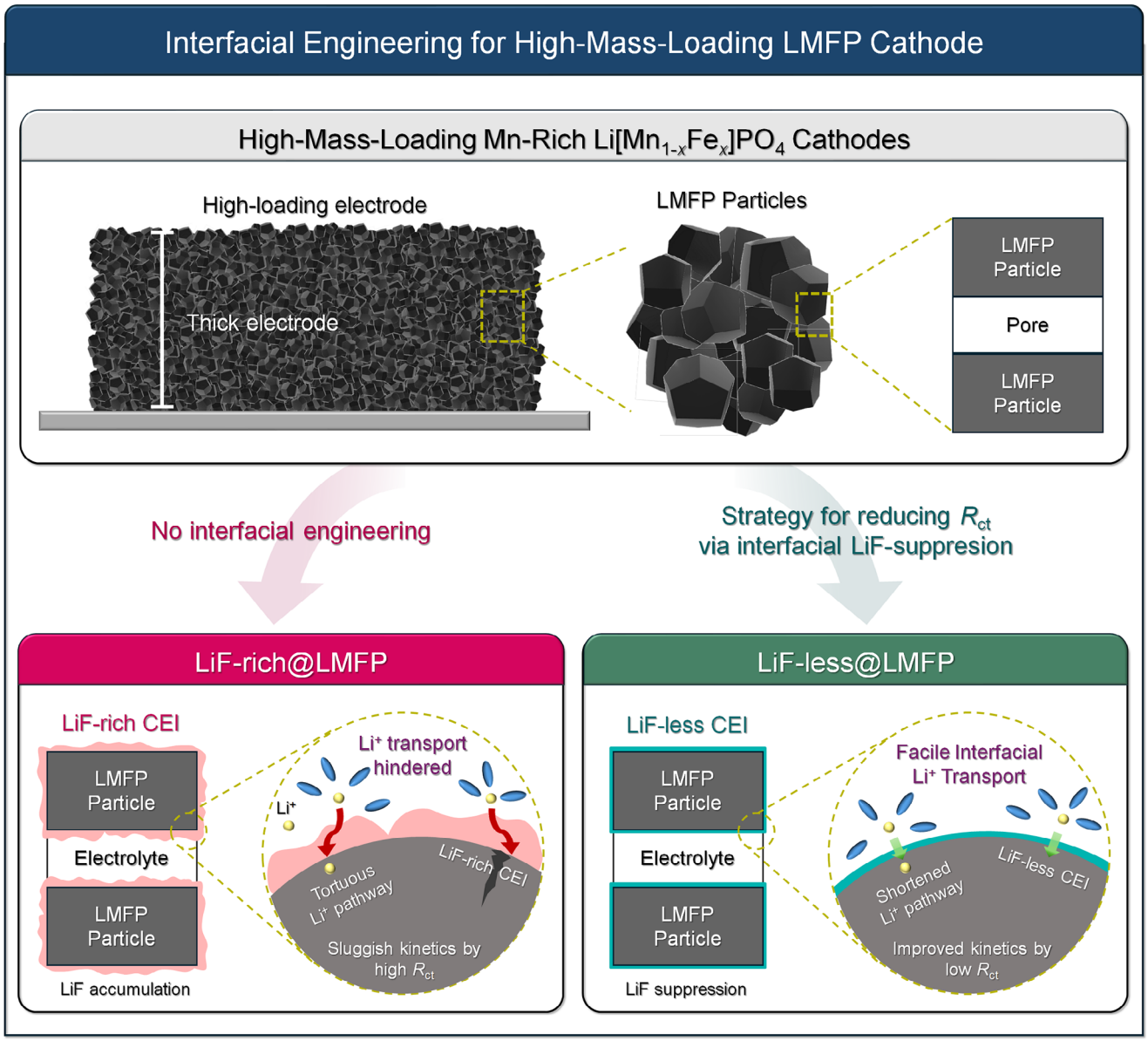

FIGURE 5 | Schematic illustration comparing LiF-rich@LMFP, in which thick LiF accumulation increases charge-transfer resistance and hinders Li^+ transport, with engineered LiF-less@LMFP, which reduces charge-transfer resistance and enables rapid Li^+ transport.

radiation ($\lambda = 0.70932$ Å), scanning over a 2θ range of 4.61°–34.32° with a step size of 0.013°. For consistency with prior literature, the diffraction patterns were converted to match Cu Kα wavelength ($\lambda = 1.54178$ Å). Structural refinement was conducted using the Foolproof software package. For *operando* measurements, XRD patterns were collected under a galvanostatic condition of 0.1C over the voltage range of 2.5–4.4 V (vs. Li^+/Li).

4.5 | Operando X-Ray Diffraction

Operando XRD measurements at a 1C charge/discharge rate were performed at beamline 9A of the Pohang Accelerator Laboratory (PAL), Korea. Monochromatic synchrotron X-rays ($\lambda = 1.13$ Å) were used, and diffraction patterns were collected in transmission mode using a CCD detector (Rayonix SX165).

4.6 | Nuclear Magnetic Resonance

^{19}F NMR spectra were recorded on a 500 MHz spectrometer (Varian Unity Inova 500), while ^{1}H, ^{13}C, ^{11}B, and ^{7}Li spectra were recorded on a 700 MHz spectrometer (Bruker AVANCE III 700). A chloroform-d (CDCl3) solution in a coaxial insert was used for lock and referencing; chemical shifts (δ) are reported in ppm.

4.7 | X-Ray Photoelectron Spectroscopy

XPS analysis was measured using an Axis Supra (Kratos, UK) at the National Center for Inter-University Research Facilities (NCIRF) at Seoul National University. All XPS spectra were acquired at the fully charged state, unless specified otherwise in the corresponding figure captions. The C–F signal in F 1*s*

XPS observed in the pristine electrode was assigned to the PVDF binder. Upon electrochemical charging, the appearance of the F–P component was attributed to fluorophosphate species derived from the $LiPF_6$-based electrolyte. To enable a more reliable assessment of the CEI composition, the cycled electrodes were not solvent-washed prior to ex situ XPS measurements, thereby retaining electrolyte-derived interfacial species.

4.8 | Time-of-Flight Secondary-Ion-Mass Spectrometry

ToF-SIMS analysis was conducted in both positive and negative ion detection modes. Depth profiling was performed using Cs^+ sputtering and Bi^{3+} analysis beams, and 3D imaging was obtained through sequential sputtering and signal accumulation. All measurements were performed under ultra-high vacuum conditions.

4.9 | Scanning Electron Microscopy

The morphology and microstructure of LMFP particles were examined using field-emission scanning electron microscopy (FE-SEM; Gemini SEM 560, ZEISS) at the National Center for Inter-University Research Facilities (NCIRF), Seoul National University.

4.10 | High-Resolution Transmission Electron Microscopy

The CEI layer thickness of LMFP was characterized via transmission electron microscopy (TEM; JEOL JEM-F200) operated at 80 keV at the Cooperative Center for Research Facilities (CCRF), Sungkyunkwan University. Prior to imaging, LMFP powder was ultrasonicated in ethanol, and a droplet of the suspension was placed on a carbon-coated Cu TEM grid. The sample was dried overnight at room temperature to evaporate the ethanol.

4.11 | Computational Details

All density functional theory (DFT) simulations were conducted using the Gaussian 16 computational package [65]. The calculations utilized a spin-unrestricted formalism in combination with the Becke–Lee–Yang–Parr (B3LYP) hybrid functional and the triple-zeta valence polarization (TZVP) basis set [66, 67]. Visualization of the molecular geometries of both electrolyte additives and solvent molecules was performed using Avogadro software [68]. To replicate the solvent environment of EC:EMC:DMC (2:4:4 by volume), a dielectric constant of 21.468 was applied, consistent with values reported in a previous study [69].

Acknowledgements

This work was supported by the Technology Innovation Program (RS-2024-00427225, Development of manufacturing process technology for 3.7 V high voltage lithium iron manganese phosphate cathode funded by the Ministry of Trade, Industry and Energy (MOTIE, Korea). This research was also supported by a National Research Council of Science & Technology (NST) grant funded by the Korea government (MSIT) (No. GTL25091-300). Furthermore, this work was supported by "Analysis of the charging behavior of LMFP cathode materials and development of strategies for fast-charging improvement" funded by LG Energy Solution.

Conflicts of Interest

The authors declare no conflicts of interest.

Data Availability Statement

The data that support the findings of this study are available from the corresponding author upon reasonable request.

References

1. M. L. Machala, X. Chen, S. P. Bunke, et al., "Life Cycle Comparison of Industrial-Scale Lithium-Ion Battery Recycling and Mining Supply Chains," *Nature Communications* 16 (2025): 988, https://doi.org/10.1038/s41467-025-56063-x.

2. J. Kim, H. Ahn, J. Ahn, et al., "Activation of Oxygen Redox by Inhibited Dynamic Phase Transition for High-Energy Li-Rich Layered Oxide Cathode," *Chemical Engineering Journal* 495 (2024): 153122, https://doi.org/10.1016/j.cej.2024.153122.

3. R. Zhang, C. Wang, P. Zou, et al., "Long-Life Lithium-Ion Batteries Realized by Low-Ni, Co-Free Cathode Chemistry," *Nature Energy* 8 (2023): 695–702, https://doi.org/10.1038/s41560-023-01267-y.

4. B. Ku, J. Ahn, H. Lee, et al., "Enhancing Structural Flexibility in P2-Type Ni-Mn-Based Na-Layered Cathodes for High Power-Capability and Fast Charging/Discharging Performance," *Energy Storage Materials* 74 (2025): 103930, https://doi.org/10.1016/j.ensm.2024.103930.

5. S.-Y. Lee, H. Kweon, S. Lee, et al., "Enhanced Fast-Discharging Performance and Cyclability in Oxygen-Redox-Based P3-Type Na-Layered Cathode via Vacancies in TM Layers," *Advanced Energy Materials* 14 (2024): 2402412, https://doi.org/10.1002/aenm.202402412.

6. S. Tang, Y. Liang, Y. Peng, et al., "Unveiling the Crucial Role of Dissolved Fe^{2+} on the Solid Electrolyte Interphase in Long-life $LiFePO_4$/Graphite Batteries," *Advanced Energy Materials* 15 (2024): 2402842, https://doi.org/10.1002/aenm.202402842.

7. R. Tang, J. Dong, C. Wang, et al., "Rate-Dependent Failure Behavior Regulation of $LiFePO_4$ Cathode via Functional Interface Engineering," *Advanced Functional Materials* 35 (2025): 2421284, https://doi.org/10.1002/adfm.202421284.

8. G. Yan, J. Wei, E. Apodaca, et al., "Identifying Critical Features of Iron Phosphate Particle for Lithium Preference," *Nature Communications* 15 (2024): 4859, https://doi.org/10.1038/s41467-024-49191-3.

9. Z. Li, M. Li, Y. Chen, et al., "Upcycling of Spent $LiFePO_4$ Cathodes to Heterostructured Electrocatalysts for Stable Direct Seawater Splitting," *Angewandte Chemie International Edition* 63 (2024): 202410396, https://doi.org/10.1002/anie.202410396.

10. S. Reed, K. Scanlan, and A. Manthiram, "Scalable, Low-Cost Synthesis of High Volumetric Capacity $LiMn_{0.5}Fe_{0.5}PO_4$ Cathode for Lithium-Ion Batteries," *Journal of Materials Chemistry A* 12 (2024): 21341–21349, https://doi.org/10.1039/d4ta03438d.

11. Y. Chen, G. Zeng, B. Zhang, et al., "From Li to Na: Exploratory Analysis of Fe-Based Phosphates Polyanion-Type Cathode Materials by Mn Substitution," *Small* 19 (2023):2303929, https://doi.org/10.1002/smll.202303929.

12. E. Xu, T. Wang, J. Chen, et al., "Stress-Induced Anomalous Lithiation Plateau of $LiFe_yMn_{1-y}PO_4$ Over High-Rate Discharging"," *Advanced Energy Materials* 15 (2024): 10, https://doi.org/10.1002/aenm.202404929.

13. G. Bree, J. Zhao, V. Majherova, et al., "Practical Pathways to Higher Energy Density LMFP Battery Cathodes," *Energy & Fuels* 39, no. 7 (2025): 3683–3689, https://doi.org/10.1021/acs.energyfuels.4c06201.

14. W. Xie, Z. Zhang, and X. Gao, "Understand Ing the Limitations of Thick Electrodes on the Rate Capability of High-Energy Density Lithium-Ion Batteries," *Electrochimica Acta* 493 (2024): 144396, https://doi.org/10.1016/j.electacta.2024.144396.

15. X. Zhang, Z. Hui, S. King, et al., "Tunable Porous Electrode Architectures for Enhanced Li-Ion Storage Kinetics in Thick Electrodes," *Nano Letters* 21 (2021): 5896–5904, https://doi.org/10.1021/acs.nanolett.1c02142.

16. J. Zhang, Y. Liu, B. Wang, and W. Yao, "Improved Electrochemical Performance of LiMn $_{0.6}$ Fe $_{0.4}$ PO $_4$ via Chitosan-Derived Nitrogen-Doped Carbon Coating," *Batteries & Supercaps* 7 (2024): 202400105, https://doi.org/10.1002/batt.202400105.

17. M. Jo, H. Yoo, Y. S. Jung, and J. Cho, "Carbon-Coated Nanoclustered $LiMn_{0.7}1Fe_{0.29}PO_4$ Cathode for Lithium-Ion Batteries," *Journal of Power Sources* 216 (2012): 162–168, https://doi.org/10.1016/j.jpowsour.2012.05.059.

18. P. Vanaphuti and A. Manthiram, "Enhancing the Mn Redox Kinetics of LiMn $_{0.5}$ Fe $_{0.5}$ PO $_4$ Cathodes Through a Synergistic Co-Doping With Niobium and Magnesium for Lithium-Ion Batteries," *Small* 20 (2024): 2404878, https://doi.org/10.1002/smll.202404878.

19. J. Peng, Z. Li, Y. You, et al., "Contribution of Ti-Doping to the Cyclic Stability of $LiFe_{0.6}Mn_{0.4}PO_4$/C," *Industrial & Engineering Chemistry Research* 63 (2024): 8228–8238, https://doi.org/10.1021/acs.iecr.4c00307.

20. H. Jin, J. Zhang, L. Qin, Y. Hu, H. Jiang, and C. Li, "Dual Modification of Olivine $LiFe_{0.5}Mn_{0.5}PO_4$ Cathodes With Accelerated Kinetics for High-Rate Lithium-Ion Batteries," *Industrial & Engineering Chemistry Research* 62 (2023): 1029–1034, https://doi.org/10.1021/acs.iecr.2c04303.

21. H. Yu, E. Zhang, J. Yu, et al., "Relaxing the Jahn–Teller Distortion of $LiMn_{0.6}Fe_{0.4}PO_4$ Cathodes via Mg/Ni Dual-Doping for High-Rate and Long-Life Li-Ion Batteries"," *Journal of Materials Chemistry A* 12 (2024): 26076, https://doi.org/10.1039/d4ta04916k.

22. H. Gao, Q. Wu, Y. Hu, J. P. Zheng, K. Amine, and Z. Chen, "Revealing the Rate-Limiting Li-Ion Diffusion Pathway in Ultrathick Electrodes for Li-Ion Batteries," *The Journal of Physical Chemistry Letters* 9 (2018): 5100–5104, https://doi.org/10.1021/acs.jpclett.8b02229.

23. T.-F. Yi, Y. Li, Z. Fang, P. Cui, S. Luo, and Y. Xie, "Improving the Cycling Stability and Rate Capability of $LiMn_{0.5}Fe_{0.5}PO_4$/C Nanorod as Cathode Materials by $LiAlO_2$ Modification," *Journal of Materiomics* 6 (2020): 33–44, https://doi.org/10.1016/j.jmat.2019.11.005.

24. J. Kim, S. Park, S. Hwang, and W.-S. Yoon, "Principles and Applications of Galvanostatic Intermittent Titration Technique for Lithium-Ion Batteries," *Journal of Electrochemical Science and Technology* 13 (2022): 19–31, https://doi.org/10.33961/jecst.2021.00836.

25. M. Choi, H. Choi, S. Park, et al., "Stabilized High-Voltage Operation of Co-Free NMX Cathode via CEI-Controlling," *Energy Storage Materials* 67 (2024): 103291, https://doi.org/10.1016/j.ensm.2024.103291.

26. C. M. E. Phelan, E. Björklund, J. Singh, et al., "Role of Salt Concentration in Stabilizing Charged Ni-Rich Cathode Interfaces in Li-Ion Batteries," *Chemistry of Materials* 36 (2024): 3334–3344, https://doi.org/10.1021/acs.chemmater.4c00004.

27. P. S. Llanos, Z. Ahaliabadeh, V. Miikkulainen, et al., "High Voltage Cycling Stability of LiF-Coated NMC811 Electrode," *ACS Applied Materials & Interfaces* 16 (2024): 2216–2230, https://doi.org/10.1021/acsami.3c14394.

28. L. Hong, Y. Zhang, P. Mei, et al., "Temperature-Responsive Formation Cycling Enabling LiF-Rich Cathode-Electrolyte Interphase," *Angewandte Chemie International Edition* 63 (2024): 202409069, https://doi.org/10.1002/anie.202409069.

29. Z. Bi, Z. Yi, L. Zhang, et al., "Ultrathin Dense LiF Coverage Coupled With a Near-Surface Gradient Fluorination Lattice Enables Fast-Charging Long-Life 4.6 V $LiCoO_2$," *Energy & Environmental Science* 17 (2024): 2765–2775, https://doi.org/10.1039/d3ee03464j.

30. S. Zhang, R. Li, N. Hu, et al., "Tackling Realistic Li(+) Flux for High-Energy Lithium Metal Batteries," *Nature Communications* 13 (2022): 5431, https://doi.org/10.1038/s41467-022-33151-w.

31. C. Seidl, S. Thieme, M. Frey, K. Nikolowski, and A. Michaelis, "Comparison of Electronic Resistance Measurement Methods and Influencing Parameters for LMFP and High-Nickel NCM Cathodes," *Batteries* 10 (2024): 105, https://doi.org/10.3390/batteries10030105.

32. Z. Lei, A. Naveed, J. Lei, et al., "High Performance Nano-Sized $LiMn_{1-x}Fe_xPO_4$cathode Materials for Advanced Lithium-Ion Batteries"," *RSC Advances* 7 (2017): 43708, https://doi.org/10.1039/c7ra08993g.

33. J. Cho, M. D. Losego, H. G. Zhang, et al., "Electrochemically Tunable Thermal Conductivity of Lithium Cobalt Oxide," *Nature Communications* 5 (2014): 4035, https://doi.org/10.1038/ncomms5035.

34. B. A. Walker, C. O. Plaza-Rivera, S.-S. Sun, W. Lu, J. W. Connell, and Y. Lin, "Dry-Pressed Lithium Nickel Cobalt Manganese Oxide (NCM) Cathodes Enabled by Holey Graphene Host," *Electrochimica Acta* 362 (2020): 137129, https://doi.org/10.1016/j.electacta.2020.137129.

35. J. Xu, K. Hou, X. Li, et al., "Enhancing the High-Rate Capability and Cycling Stability of $LiMn_{0.6}Fe_{0.4}PO_4$/C Cathode Materials for Lithium-Ion Batteries by Na^+ Doping," *ACS Applied Energy Materials* 7 (2024): 8694–8704, https://doi.org/10.1021/acsaem.4c01659.

36. X. Gao, Y.-N. Zhou, D. Han, et al., "Thermodynamic Understand Ing of Li-Dendrite Formation," *Joule* 4 (2020): 1864–1879, https://doi.org/10.1016/j.joule.2020.06.016.

37. M. Ryu, Y. K. Hong, S. Y. Lee, and J. H. Park, "Ultrahigh Loading Dry-Process for Solvent-Free Lithium-Ion Battery Electrode Fabrication," *Nature Communications* 14 (2023): 1316, https://doi.org/10.1038/s41467-023-37009-7.

38. Y. Meng, Y. Wang, Z. Zhang, X. Chen, Y. Guo, and D. Xiao, "A Phytic Acid Derived $LiMn_{0.5}Fe_{0.5}PO_4$/Carbon Composite of High Energy Density for Lithium Rechargeable Batteries," *Scientific Reports* 9 (2019): 6665, https://doi.org/10.1038/s41598-019-43140-7.

39. L.-L. Lu, Y.-Y. Lu, Z.-X. Zhu, et al., "Extremely Fast-Charging Lithium Ion Battery Enabled by Dual-Gradient Structure Design," *Science Advances* 8 (2022): abm6624, https://doi.org/10.1126/sciadv.abm6624.

40. R. George, K. T. Kashyap, R. Rahul, and S. Yamdagni, "Strengthening in Carbon Nanotube/Aluminium (CNT/Al) Composites," *Scripta Materialia* 53 (2005): 1159, https://doi.org/10.1016/j.scriptamat.2005.07.022.

41. N. Meng, X. Ren, G. Santagiuliana, et al., "Ultrahigh β-Phase Content Poly(Vinylidene Fluoride) With Relaxor-Like Ferroelectricity for High Energy Density Capacitors," *Nature Communications* 10 (2019): 4535, https://doi.org/10.1038/s41467-019-12391-3.

42. Y. Luo, Y. Chen, N. Koratkar, and W. Liu, "Densification of Alloying Anodes for High Energy Lithium-Ion Batteries: Critical Perspective on Inter- Versus Intra-Particle Porosity," *Advanced Science* 11 (2024): 2403530, https://doi.org/10.1002/advs.202403530.

43. B. Zhang, W. Meng, Y. Gong, et al., "[001]-Oriented $LiMn_{0.6}Fe_{0.4}PO_4$/C Nanorod Microspheres Contributing High-Rate Performance to Olivine-Structured Cathode for Lithium-Ion Battery," *Materials Today Energy* 30 (2022): 101162, https://doi.org/10.1016/j.mtener.2022.101162.

44. R. A. Huggins and W. Weppner, "Electrochemical Investigation of the Chemical Diffusion, Partial Ionic Conductivities, and Other Kinetic Parameters in Li_3Sb and Li_3Bi," *Journal of Solid State Chemistry* 22 (1977): 297–308, https://doi.org/10.1016/0022-4596(77)90006-8.

45. A. P. Nowak, B. Wicikowska, K. Trzciński, and A. Lisowska-Oleksiak, "Determination of Chemical Diffusion Coefficient of Lithium Ions in Ceramics Derived From Pyrolysed Poly(1,2-dimethylsilazane) and Starch," *Procedia Engineering* 98 (2014): 8–13, https://doi.org/10.1016/j.proeng.2014.12.480.

46. S. D. Talian, S. Brutti, M. A. Navarra, J. Moškon, and M. Gaberscek, "Impedance Spectroscopy Applied to Lithium Battery Materials: Good Practices in Measurements and Analyses," *Energy Storage Materials* 69 (2024): 103413, https://doi.org/10.1016/j.ensm.2024.103413.

47. R. Sahore, D. C. O'Hanlon, A. Tornheim, et al., "Revisiting the Mechanism behind Transition-Metal Dissolution From Delithiated $LiNi_xMn_yCo_zO_2$ (NMC) Cathodes," *Journal of The Electrochemical Society* 167 (2020): 020513, https://doi.org/10.1149/1945-7111/ab6826.

48. S. Zhao, F. Wu, L. Yang, L. Gao, and A. F. Burke, "A Measurement Method for Determination of Dc Internal Resistance of Batteries and Supercapacitors," *Electrochemistry Communications* 12 (2010): 242–245, https://doi.org/10.1016/j.elecom.2009.12.004.

49. M. Jiao, P. Huang, Z. Pang, et al., "Uncovering the Battery Direct Current Internal Resistance Puzzle: A Machine Learning-driven Pore Network Approach," *Journal of Power Sources* 628 (2025): 235891, https://doi.org/10.1016/j.jpowsour.2024.235891.

50. X. Liu, M. Gao, J. Zhao, et al., "Effects of Charging Protocols on the Cycling Performance for High-Energy Lithium-Ion Batteries Using a Graphite-SiOx Composite Anode and Li-Rich Layered Oxide Cathode," *Journal of Power Sources* 495 (2021): 229793, https://doi.org/10.1016/j.jpowsour.2021.229793.

51. K. Shin, H. Moon, G. Kang, et al., "Interfacial Engineering Using a Thiophene-Based Electrolyte Additive for High-Voltage Lithium-Ion Batteries," *Energy & Fuels* 39 (2025): 4525–4539, https://doi.org/10.1021/acs.energyfuels.4c06415.

52. Z. Zhang, F. Liu, Z. Huang, et al., "Enhancing the Electrochemical Performance of a High-Voltage $LiCoO_2$ Cathode With a Bifunctional Electrolyte Additive," *ACS Applied Energy Materials* 4 (2021): 12954–12964, https://doi.org/10.1021/acsaem.1c02593.

53. C. Yan, Y. Xu, J. Xia, C. Gong, and K. Chen, "Tris(trimethylsilyl) Borate as an Electrolyte Additive for High-Voltage Lithium-Ion Batteries Using $LiNi_{1/3}Mn_{1/3}Co_{1/3}O_2$ Cathode," *Journal of Energy Chemistry* 25 (2016): 659–666, https://doi.org/10.1016/j.jechem.2016.04.010.

54. J. Lan, H. Hou, X. Yu, J. Rong, and B. Huang, "Insights Into the Role of $Li_2FeP_2O_7$ Phase in $LiFePO_4$/C Composite Cathode," *Ionics* 28 (2022): 5059–5069, https://doi.org/10.1007/s11581-022-04760-8.

55. L.-L. Lu, Z.-X. Zhu, T. Ma, et al., "Superior Fast-Charging Lithium-Ion Batteries Enabled by the High-Speed Solid-State Lithium Transport of an Intermetallic Cu_6Sn_5 Network," *Advanced Materials* 34 (2022): 2202688, https://doi.org/10.1002/adma.202202688.

56. J. P. Allen and C. P. Grey, "Solution NMR of Battery Electrolytes: Assessing and Mitigating Spectral Broadening Caused by Transition Metal Dissolution," *The Journal of Physical Chemistry C* 127 (2023): 4425–4438, https://doi.org/10.1021/acs.jpcc.2c08274.

57. M. Sieland, M. Schenker, L. Esser, B. Kirchner, and B. M. Smarsly, "Ionic Liquid-Based Low-Temperature Synthesis of Crystalline $Ti(OH)OF{\cdot}0.66H_2O$: Elucidating the Molecular Reaction Steps by NMR Spectroscopy and Theoretical Studies," *ACS Omega* 7 (2022): 5350–5365, https://doi.org/10.1021/acsomega.1c06534.

58. N. R. Park, M. Zhang, B. Han, et al., "Understanding Boron Chemistry as the Surface Modification and Electrolyte Additive for Co-Free Lithium-Rich Layered Oxide," *Advanced Energy Materials* 14 (2024): 2401968, https://doi.org/10.1002/aenm.202401968.

59. X. Deng, M. Hu, X. Wei, et al., "Nuclear Magnetic Resonance Studies of the Solvation Structures of a High-Performance Nonaqueous Redox Flow Electrolyte," *Journal of Power Sources* 308 (2016): 172–179, https://doi.org/10.1016/j.jpowsour.2015.12.005.

60. M. V. Kaplanskiy, D. A. Shitov, P. M. Tolstoy, and E. Y. Tupikina, "Deconstructing ^{1}H NMR Chemical Shifts in Strong Hydrogen Bonds: A Computational Investigation of Solvation, Dynamics, and Nuclear Delocalization Effects," *Journal of Chemical Information and Modeling* 65 (2025): 5019–5034, https://doi.org/10.1021/acs.jcim.5c00566.

61. M. Kim, H. Moon, S. Kim, et al., "Tunable Solvation Structures for Fast Charging of Micron-Si Anodes in Energy-Dense Lithium-Ion Batteries," *Chemical Engineering Journal* 511 (2025): 162079, https://doi.org/10.1016/j.cej.2025.162079.

62. S. Park, G. Choi, H. Y. Lim, et al., "A Phosphorofluoridate-Based Multifunctional Electrolyte Additive Enables Long Cycling of High-Energy Lithium-Ion Batteries," *ACS Applied Materials & Interfaces* 15 (2023): 33693–33702, https://doi.org/10.1021/acsami.3c06882.

63. D. B. Ravnsbæk, K. Xiang, W. Xing, et al., "Engineering the Transformation Strain in $LiMn_yFe_{1-y}PO_4$ Olivines for Ultrahigh Rate Battery Cathodes," *Nano Letters* 16 (2016): 2375–2380, https://doi.org/10.1021/acs.nanolett.5b05146.

64. H. Zhu, Z. Li, C. Li, et al., "Near-In-Situ Electrochemical Impedance Spectroscopy Analysis Based on Lithium Iron Phosphate Electrode," *Electrochimica Acta* 464 (2023): 142919, https://doi.org/10.1016/j.electacta.2023.142919.

65. M. Frisch, G. Trucks, and H. Schlegel, *Gaussian Inc 16, Revision A. 03* (Gaussian Inc., 2016).

66. A. Schäfer, C. Huber, and R. Ahlrichs, "Fully Optimized Contracted Gaussian Basis Sets of Triple Zeta Valence Quality for Atoms Li to Kr," *The Journal of Chemical Physics* 100, no. 8 (1994): 5829–5835, https://doi.org/10.1063/1.467146.

67. A. Schiafer, H. Horn, and R. Ahlrichs, "Fully Optimized Contracted Gaussian Basis Sets for Atoms Li to Kr," *Journal of Chemical Physics* 97 (1992): 2571.

68. M. D. Hanwell, D. E. Curtis, D. C. Lonie, T. Vandermeersch, E. Zurek, and G. R. Hutchison, "Avogadro: An Advanced Semantic Chemical Editor, Visualization, and Analysis Platform," *Journal of Cheminformatics* 4 (2012): 17, https://doi.org/10.1186/1758-2946-4-17.

69. D. S. Hall, J. Self, and J. R. Dahn, "Dielectric Constants for Quantum Chemistry and Li-Ion Batteries: Solvent Blends of Ethylene Carbonate and Ethyl Methyl Carbonate," *The Journal of Physical Chemistry C* 119 (2015): 22322–22330, https://doi.org/10.1021/acs.jpcc.5b06022.

Supporting Information

Additional supporting information can be found online in the Supporting Information section.

Supporting File: aenm70680-sup-0001-SuppMat.docx.